

GBT Exploratory Time Observations of the Double-Pulsar System PSR J0737–3039

S. Ransom

Dept. of Physics, McGill University, 3600 University St., Montreal, QC H3A 2T8, Canada

P. Demorest

Dept. of Astronomy and Radio Astronomy Laboratory, University of California at Berkeley, 601 Campbell Hall 3411, Berkeley, CA 94720

V. Kaspi

Dept. of Physics, McGill University, 3600 University St., Montreal, QC H3A 2T8, Canada

R. Ramachandran, D. Backer

Dept. of Astronomy and Radio Astronomy Laboratory, University of California at Berkeley, 601 Campbell Hall 3411, Berkeley, CA 94720

Abstract. We report results from Exploratory Time observations of the double-pulsar system PSR J0737–3039 using the Green Bank Telescope (GBT). The large gain of the GBT, the diversity of the pulsar backends, and the four different frequency bands used have allowed us to make interesting measurements of a wide variety of phenomena. Here we briefly describe results from high-precision timing, polarization, eclipse, scintillation velocity, and single-pulse work.

1. Introduction

In December 2003, we proposed for and were awarded Exploratory Time to observe the spectacular double-pulsar system PSR J0737–3039 (hereafter 0737; Burgay et al. 2003, Lyne et al. 2004, and contributions to this volume from Burgay, Manchester, Kramer, and others) as part of the NRAO Rapid Response Science program¹. We observed 0737 five times at four different frequencies (427, 2×820, 1400, and 2200 MHz) using the Berkeley-Caltech Pulsar Machine (BCPM) and the Green Bank Pulsar Processor (GBPP; which measures full polarization information). For two of the observations (one each at 427 and 820 MHz) we also used the new GBT Spectrometer SPIGOT card (a correlator-

¹<http://www.vla.nrao.edu/astro/prop/rapid/>

based instrument that outputs lags at 25 MB/s) in some of its first scientific observations. These data are public and can be obtained from NRAO.

2. High-precision Timing

The high sensitivity of the GBT allowed us to measure high signal-to-noise ratio (SNR) pulse profiles from PSR J0737–3039A (hereafter PSR A, see Fig. 1) at each observing frequency, precise ($\lesssim 11 \mu\text{s}$) pulse arrival times (TOAs) from PSR A in 1–2 min integrations, and TOAs throughout $\sim 80\%$ of the orbit for PSR J0737–3039B (hereafter PSR B). Without a long timing baseline we could only measure “local” parameters, such as the Shapiro delay “shape” $s \equiv \sin i$ for PSR A, and better projected orbital semi-major axes $x \equiv a \sin i/c$ for the pulsars.

For PSR A we used the Lyne et al. (2004) ephemeris as our base and extracted TOAs from the high SNR 820- and 1400-MHz BCPM and SPIGOT observations. Using TEMPO², we determined $s = 0.99962^{+0.00038}_{-0.00095}$ (corresponding to $i = 88^\circ 4^{+1.6}_{-1.4}$) and $x_A = 1.4150342(82)$ lt-sec with a post-fit RMS of $\sim 11 \mu\text{s}$ (the SPIGOT data alone had an RMS of $\lesssim 7 \mu\text{s}$). The errors for s and x_A were estimated using a bootstrap analysis. We note that we had to fit out apparent linear arrival time drifts of order tens of μs during each of the observations. We believe that these (likely) systematic drifts could result from uncorrected variations in the linearly polarized portion of the pulse profile due to the rotation of the receiver feed with respect to the sky and gain differences between the two orthogonally polarized IFs. See Ransom et al. (2004) for more details of the PSR A timing.

To time PSR B, we determined a set of 29 template profiles (all referenced to the same Gaussian component) as a function of the orbital phase (since PSR B’s pulse profile changes systematically throughout the orbit) and extracted TOAs from each of the BCPM observations. Using the Lyne et al. (2004) timing solution as a starting point, we used TEMPO to fit only for x_B and the local spin frequency. The post-fit residuals show significant systematics as a function of orbital phase (see Fig. 3), implying that there may be no stable timing reference point in the varying profile (i.e. PSR A’s wind likely affects the radio beam of PSR B as a function of orbital phase). If we multiply TEMPO’s formal errors on x_B by 10.3 (the square-root of the reduced- χ^2 of the fit) to try and account for some of these systematics, we get $x_B = 1.5126(14)$ lt-sec and a mass ratio $R \equiv m_A/m_B = x_B/x_A = 1.06893(97)$, which is a factor of ~ 6 more precise than reported in Lyne et al. (2004). A M_A vs. M_B diagram based on the GBT data but using the reported value of $\dot{\omega}$ from Lyne et al. (2004) is shown in Figure 1.

²<http://pulsar.princeton.edu/tempo>

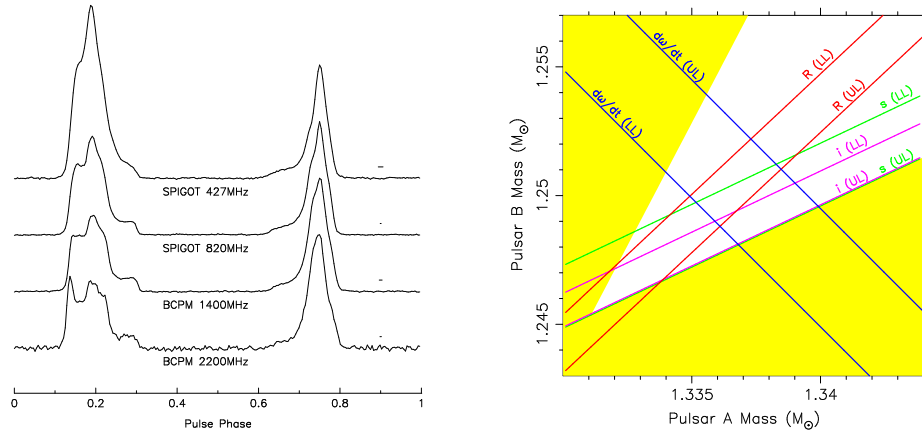


Figure 1. (Left) Average pulse profiles of PSR A from the GBT. Changes in the relative pulse amplitudes with observing frequency are obvious. The short lines above and to the right of the profiles depict the time resolution of the data. (Right) A diagram of the M_A vs. M_B plane (after Lyne et al. 2004) based on the GBT data (except for the advance of periastron $\dot{\omega}$). The shaded region requires an inclination $i > 90^\circ$ and is therefore not allowed. The other plotted parameters are the mass ratio $R \equiv m_A/m_B$, the Shapiro delay “shape” parameter $s \equiv \sin i$, and the i as determined using both timing (§2.) and scintillation measurements (§5.). Lower and upper limits on the various parameters are labeled with LL or UL respectively.

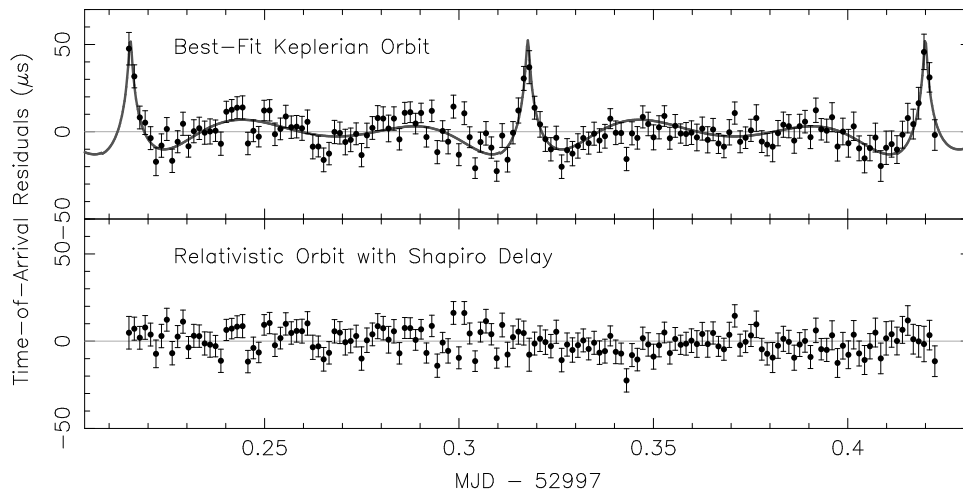


Figure 2. Timing residuals from the 820 MHz SPIGOT observation of PSR A before (top) and after (bottom) the addition of a Shapiro delay “shape” fit for a $1.25 M_\odot$ companion. The Shapiro delay is easily detected during *each* orbit. The post-fit RMS residuals for these data alone are $\lesssim 7 \mu\text{s}$.

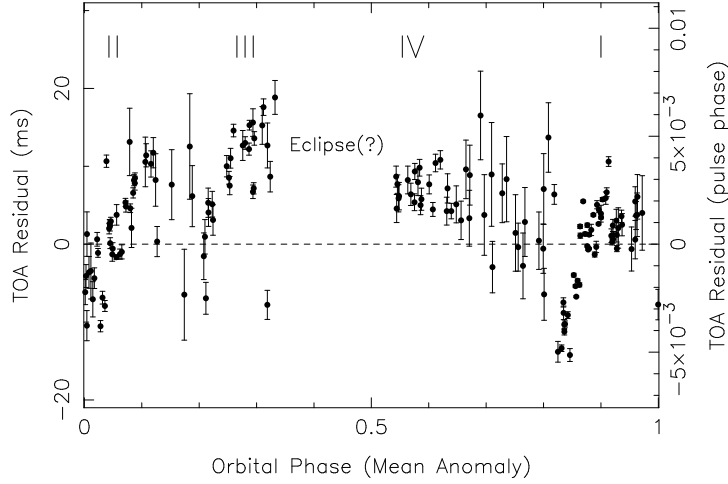


Figure 3. Post-fit timing residuals as a function of orbital phase for PSR B. The only fit parameters were the projected semi-major axis x_B and the spin frequency. The TOAs are from BCPM data from all five GBT observations of 0737. Systematic drifts in the TOAs are obvious, even after using orbital-phase-dependent profile templates to extract the TOAs. The “bright” portions of the orbit as defined in Demorest et al. (2004) and Ramachandran et al. (2004) are labeled as I, II, III, and IV. The possible “eclipse” of PSR B is also indicated (see §6.).

3. Polarization

The GBPP coherently dedisperses and folds full-Stokes data on a single pulsar in real time. The most useful polarimetric data sets were those taken at 820 MHz: PSR B on 2003 Dec 19 and PSR A on 2003 Dec 24. We used the full track on PSR A to perform polarization self calibration of the data. This calibration fit included terms accounting for channel gain difference, feed cross coupling, feed ellipticity, and cable delays. The RMS average of all such off-diagonal Mueller matrix elements was 0.085, so we are confident that our calibration is fairly good. We also used measurements of the observatory correlated noise source and observations of PSR B1929+10 to confirm our calibration.

Figure 4 shows the 820 MHz GBPP observations of PSR A and the mirror-like symmetry of the pulse profile. We have chosen longitude $\phi = 0$ as the center of this symmetry, which is visible in both the total power and linearly polarized profiles. Also shown is the position angle versus pulse longitude for points having $>4\sigma$ significance. The longitude region $-100^\circ < \phi < -70^\circ$ appears to contain an orthogonal emission mode jump. The region $+90^\circ < \phi < +105^\circ$ may also be affected by quasi-orthogonal modes. We find the rotation measure of this pulsar to be $-112.3 \pm 1.5 \text{ rad m}^{-2}$.

The mirror symmetry of the profile suggests that the emission is coming from two traversals of a wide, hollow emission cone, rather than from two opposite magnetic poles. We have performed a rotating vector model (RVM; Radhakrishnan & Cooke 1969) fit to the data which seems to support this interpretation. The fit gives values for the angle between the magnetic and rotation axes (α)

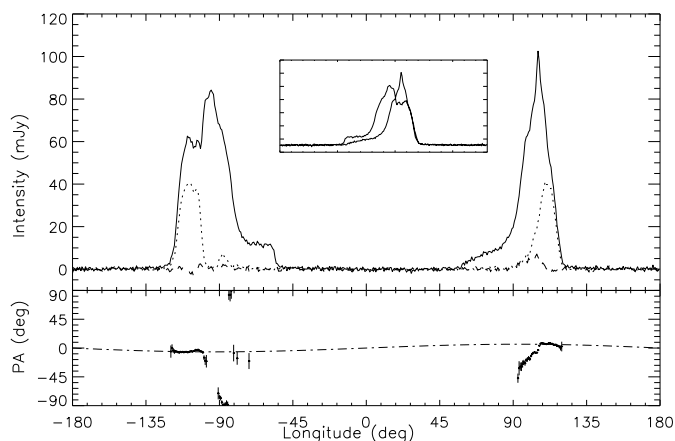


Figure 4. (Top) GBPP 820 MHz profiles of PSR A. The dotted and dashed lines show linear and circular polarization respectively, while the solid line is the total intensity. The mirror-like symmetry of the profile (see inset) implies that the pulses come from two crossings of a single cone of emission. (Bottom) A rotating vector model (RVM) fit to the data (see §3.). See Demorest et al. (2004) for more details.

and the closest angle between the magnetic axis and the line of sight (β). We can also calculate the cone opening half-angle ρ , using the longitude separation of the two peaks. The fit produces two solutions, one with $\alpha = 4^\circ \pm 3^\circ$ and one with $\alpha = 90^\circ \pm 10^\circ$. The large- α solution requires an extremely large opening angle, $\rho \sim 90^\circ$. We favor the small- α solution, as it is more consistent with the mirror symmetry, and permits more modest values of ρ . In this solution, β is unconstrained, although we argue that it is likely that $\beta \sim \rho$.

The polarimetric properties of PSR B are also interesting, though less easily understood. In addition to showing a remarkable intensity variation throughout its orbit, this pulsar shows variation in its degree of linear polarization. The brightest “window” (I), just before conjunction, shows a peak linear polarization fraction of $\sim 14\%$. However, in the next bright window (II), just after conjunction, the pulse is almost completely unpolarized ($\lesssim 1\%$). From window I, we determine the rotation measure to be $-118 \pm 12 \text{ rad m}^{-2}$, consistent with our value for PSR A. More details on these observations, the model fits, and their implications are given in Demorest et al. (2004).

4. Eclipses of PSR A

We used the BCPM data to study the eclipse of PSR A. We folded data obtained within 2 min of PSR A’s superior conjunction in 2-s intervals using 256 phase bins and then cross-correlated each profile with a template. The cross-correlation, done in the Fourier domain, assumes the data profile p has the form $p(j) = a + b \times s(j - \tau) + n(j)$, for $1 < j < 256$, and where $s(j)$ is the template, b is a scale factor, $n(j)$ is the noise background, and τ is a temporal offset. Values of a , b and τ were adjusted iteratively to minimize a χ^2 fit to each profile (Taylor

1990). We used the scale factor b and its standard deviation as a relative measure of the pulsar’s flux and its uncertainty, respectively. Our resulting eclipse light curves at three radio frequencies are presented in Figure 5. The eclipse properties are remarkably independent of frequency, as previously noted qualitatively by Lyne et al. (2004). Because of its largely achromatic properties, we show in Figure 5d an eclipse light curve obtained by averaging those in panels a, b, and c. A striking eclipse property is that it is asymmetric at all frequencies in a similar way. The eclipse ingress is clearly longer in duration than the egress.

To quantify some of these properties, we fit the light curves with two functions of the form $F(\phi) = (e^{(\phi-\phi_0)/w} + 1)^{-1}$, where $F(\phi)$ is the flux at orbital phase ϕ , defined such that superior conjunction is at $\phi = 0$. The best fits are shown as solid curves in Figure 5 and all yield values of reduced- χ^2 near unity. Using the fit parameters, we quantitatively show that the eclipse duration is independent of frequency with a limit on a power-law index of ~ 0.5 ; that the ingress takes ~ 3 times longer than egress, and that the eclipse very likely lasts longer post-conjunction. There is a hint that the eclipse asymmetry grows with increasing radio frequency, but this is not statistically significant.

A possible model for the PSR A eclipse is presented by Arons et al. (in this volume; see also Arons et al., in preparation). PSR A’s wind likely confines PSR B’s magnetosphere on the side facing PSR A, causing it to resemble a time-dependent variant of the Earth’s magnetosphere. Synchrotron absorption in a shock heated “magnetosheath” surrounding and containing PSR B’s magnetosphere is then responsible for the eclipse. Additional details on the data analysis and the eclipse model can be found in Kaspi et al. (2004).

5. Scintillation Velocity

The high SNR of the GBT data at 1400 MHz and the fantastic frequency resolution of the SPIGOT at 820 MHz allowed us to make “self-calibrating” measurements of the orbital variation of the diffractive scintillation timescale Δt_d for PSR A and hence, the so-called scintillation velocity $V_{\text{ISS}} \propto 1/\Delta t_d$ (e.g., Cordes & Rickett 1998). Closely following the methodology of Ord et al. (2004), we computed dynamic spectra for PSR A for the two observations (see Fig. 6), and then using the known (from timing) orbital motion of PSR A, fit a model consisting of four parameters: the orbital inclination i , the systemic velocity parallel- (V_{plane}) and perpendicular-to (V_{perp}) the line of nodes on the sky, and the scaling parameter κ . Our results indicate that 0737 is moving across the sky at $V_{\text{ISS}} \simeq 140.9 \pm 6.2 \text{ km s}^{-1}$, with component velocities of $V_{\text{plane}} \simeq 96.0 \pm 3.7 \text{ km s}^{-1}$ and $V_{\text{perp}} \simeq 103.1 \pm 7.7 \text{ km s}^{-1}$. When combined with the timing fits described in §2., the best-fit inclination is $i = 88^\circ 7 \pm 0^\circ 9$.

Using a simple kinematic argument and estimates of the characteristics of 0737 before the second supernova (Dewi & van den Heuvel 2004; Willems & Kalogera 2004), the large V_{perp} implies that PSR B was born with a kick of $\gtrsim 100 \text{ km s}^{-1}$. Future measurements of the scintillation velocity should allow us to remove the contaminating effects of the Earth’s motion around the Sun and the differential rotation of the Galaxy. A precise systemic velocity in combination with a VLBA-determined proper motion will provide an accurate geometric distance to the

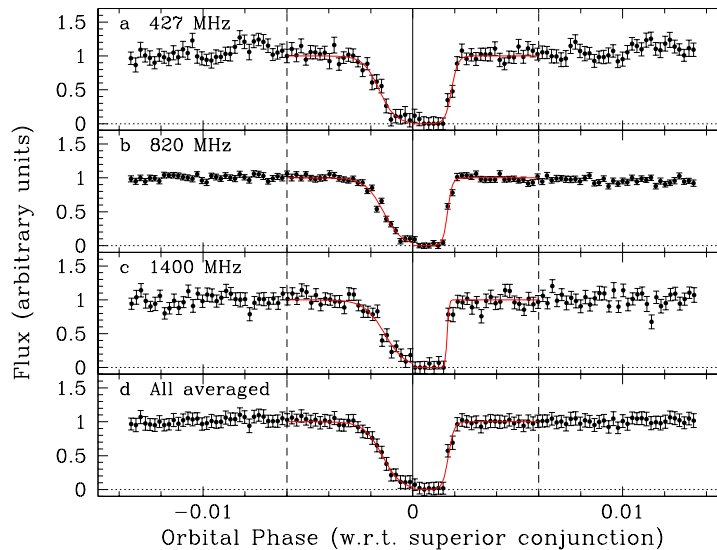


Figure 5. Plots of the eclipses of PSR A at 427-, 820- and 1400-MHz with a time resolution of ~ 2 s. The asymmetric ingress and egress of the eclipses and its near frequency independence are obvious. The deepest (i.e. most complete) part of the eclipse occurs just after conjunction.

system (which could be crucial for high precision tests of gravitational theories; see the contribution by Kramer in this volume). See Ransom et al. (2004) for more details.

6. Pulse Fluctuations and Morphology

Thanks to the superior sensitivity of the GBT, we detected PSR B at good signal-to-noise levels almost throughout the orbit. Figure 7 shows the normalized flux received from PSR B as a function of the true anomaly (referenced from the line of nodes) ϕ_{orb} , at 820- (filled circles) and 1400-MHz (open circles). The light curve shows significant systematic variation, as first shown by Lyne et al. (2004), and four prominent phase windows where the pulsar is bright (indicated by I, II, III & IV; see also Fig. 3). In the range of $\phi_{\text{orb}} \sim 6^\circ$ to 65° , the pulsar appears to exhibit what may be interpreted as an eclipse, where we did not detect any signal within our sensitivity limits. In fact, around the eclipse boundary, the reduction in SNR was so significant that the pulsar became undetectable within a few rotation periods of PSR B. The magnetopause model of Arons et al. (this volume) may be able to explain at least some of PSR B’s systematic flux variation (including the eclipse), as well as PSR A’s eclipse (Jenet & Ransom 2004; see also the contribution from Jenet in this volume) propose an alternate model for PSR B’s flux variation where PSR B brightens when it is illuminated by the cone of (presumably high-energy or particle) emission from PSR A.

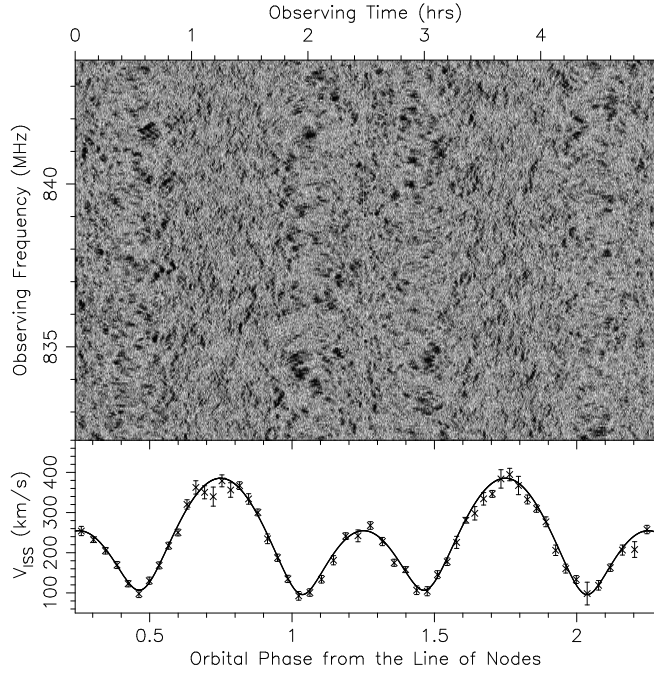


Figure 6. Dynamic spectra (top) and a scintillation velocity model fit (bottom) for the 820-MHz SPIGOT observation. Only the top 1/4 of the band is plotted. The fit implies that 0737 is moving across the sky at $\sim 140 \text{ km s}^{-1}$. See §5. and Ransom et al. (2004) for more details.

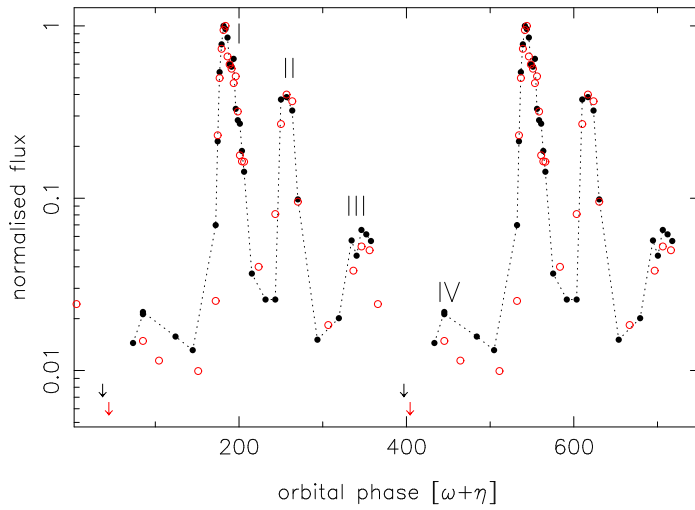


Figure 7. 820- (filled circles) and 1400-MHz (open circles) orbital lightcurve of PSR B. See §6. and Ramachandran et al. (2004) for details.

Both PSR A and PSR B exhibit significant intrinsic pulse to pulse variations. The measured modulation index m at 820 MHz as a function of pulse longitude for PSR A is in the range 0.6–2.0. PSR B’s profile structure is much more complex, where even the average profile changes systematically as a function of ϕ_{orb} (as first discussed by Lyne et al. 2004), presumably indicating a change in the emission beam morphology. In windows I and II, values of m are in the range 1–1.5 and 1–2, respectively. These values are significantly greater than what is expected from interstellar scattering ($\sim 7\%$), given the measured frequency and temporal dimensions of scintles and their filling factor (Ransom et al. 2004). The spectral shape of these intrinsic fluctuations are “noiselike” (i.e. white), indicating the lack of any organized drifting patterns. We present a much more detailed study of the above mentioned properties in Ramachandran et al. (2004).

7. Conclusion

The fantastic and highly-varied science to come from these five observations gives some indication of how important a role the GBT will play in future work on 0737. These observations provide the best constraints yet available on the inclination of the orbits, the mass ratio of the pulsars, the geometry of PSR A’s radio emission, the asymmetries and achromaticity of PSR A’s eclipses (and the nature of PSR B’s magnetosphere that cause them), the orbital modulation of PSR B’s pulsed flux, and the systemic velocity of 0737 and the natal kick.

The high gain of the telescope, the availability of many sensitive and useful receivers, and the new pulsar backends (including the SPIGOT and two coherent de-dispersion systems) will ensure that these are only the first of a long series of GBT-based results from the double-pulsar.

Acknowledgments. Special thanks go to Fred Rasio for allowing us to include this talk in the program at the very last moment.

References

- Burgay, M., et al. 2003, *Nature*, 426, 531
 Cordes, J. M., & Rickett, B. J. 1998, *ApJ*, 507, 846
 Demorest, P., et al. 2004, *ApJ*, 615, L137
 Dewi, J. D. M., & van den Heuvel, E. P. J. 2004, *MNRAS*, 349, 169
 Jenet, F. A., & Ransom, S. M. 2004, *Nature*, 428, 919
 Kaspi, V. M., et al. 2004, *ApJ*, 613, L137
 Lyne, A. G., et al. 2004, *Science*, 303, 1153
 Ord, S. M., Bailes, M., & van Straten, W. 2002, *ApJl*, 574, L75
 Radhakrishnan, V., & Cooke, D. J. 1969, *Ann. Phys. (Leipzig)*, 3, 225
 Ramachandran, R., Backer, D. C., Demorest, P., Ransom, S. M., & Kaspi, V. M. 2004, *ApJ*, in press
 Ransom, S. M., et al. 2004, *ApJ*, 609, L71
 Taylor, J. H. 1990, in *Impact of Pulsar Timing on Relativity and Cosmology*, ed. D. C. Backer (Berkeley: Center for Particle Astrophysics), m1
 Willems, B., & Kalogera, V. 2004, *ApJl*, 603, L101